

Semi-Supervised Biomedical Image Segmentation via Diffusion Models and Teacher-Student Co-Training

Luca Ciampi^{a,*}, Gabriele Lagani^{a,*}, Giuseppe Amato^a, Fabrizio Falchi^a

^aISTI-CNR, Pisa, Italy

Abstract

Supervised deep learning for semantic segmentation has achieved excellent results in accurately identifying anatomical and pathological structures in medical images. However, it often requires large annotated training datasets, which limits its scalability in clinical settings. To address this challenge, semi-supervised learning is a well-established approach that leverages both labeled and unlabeled data. In this paper, we introduce a novel semi-supervised teacher-student framework for biomedical image segmentation, inspired by the recent success of generative models. Our approach leverages denoising diffusion probabilistic models (DDPMs) to generate segmentation masks by progressively refining noisy inputs conditioned on the corresponding images. The teacher model is first trained in an unsupervised manner using a cycle-consistency constraint based on noise-corrupted image reconstruction, enabling it to generate informative semantic masks. Subsequently, the teacher is integrated into a co-training process with a twin-student network. The student learns from ground-truth labels when available and from teacher-generated pseudo-labels otherwise, while the teacher continuously improves its pseudo-labeling capabilities. Finally, to further enhance performance, we introduce a multi-round pseudo-label generation strategy that iteratively improves the pseudo-labeling process. We evaluate our approach on multiple biomedical imaging benchmarks, spanning multiple imaging modalities and segmentation tasks. Experimental results show that our method consistently outperforms state-of-the-art semi-supervised techniques, highlighting its effectiveness in scenarios with limited annotated data. The code to replicate our experiments can be found at https://github.com/ciampluca/diffusion_semi_supervised_biomedical_image_segmentation

Keywords: Biomedical Imaging, Semi-supervised learning, Diffusion Models, Semantic Segmentation, Generative Models

1. Introduction

Semantic segmentation in biomedical imaging involves assigning a classification label to each pixel, allowing for the precise identification of structures such as cells, tumors, and lesions. This process is instrumental in advancing computer-aided diagnosis by automating the detection and delineation of critical anatomical and pathological regions. In recent years, deep learning models (DL), particularly those leveraging convolutional neural networks (CNNs) and transformers, have demonstrated exceptional performance in this domain [1, 2, 3, 4, 5, 6, 7, 8, 9]. However, these methods typically require large volumes of annotated train-

ing data to enable supervised learning via backpropagation. The reliance on manually labeled datasets presents a major obstacle to their widespread adoption, as the annotation process is both time-consuming and resource-intensive, constraining their applicability in large-scale clinical settings [10, 11, 12, 13, 14, 15].

To address this limitation, significant research efforts have been dedicated to developing training strategies to cope with the limited label availability, integrating standard supervised learning with additional training on unlabeled data, i.e., semi-supervised learning [16, 17, 18, 19, 20, 21, 22]. Among semi-supervised learning approaches, teacher-student methods have proven to be particularly effective [23, 24, 25]. In this framework, a student network learns from ground-truth labels when available, while relying on pseudo-labels generated by a separate teacher model otherwise. It is important to acknowledge that these pseudo-labels are not always ac-

*Corresponding authors. They contribute equally to this work.

Email addresses: luca.ciampi@isti.cnr.it (Luca Ciampi), gabriele.lagani@isti.cnr.it (Gabriele Lagani)

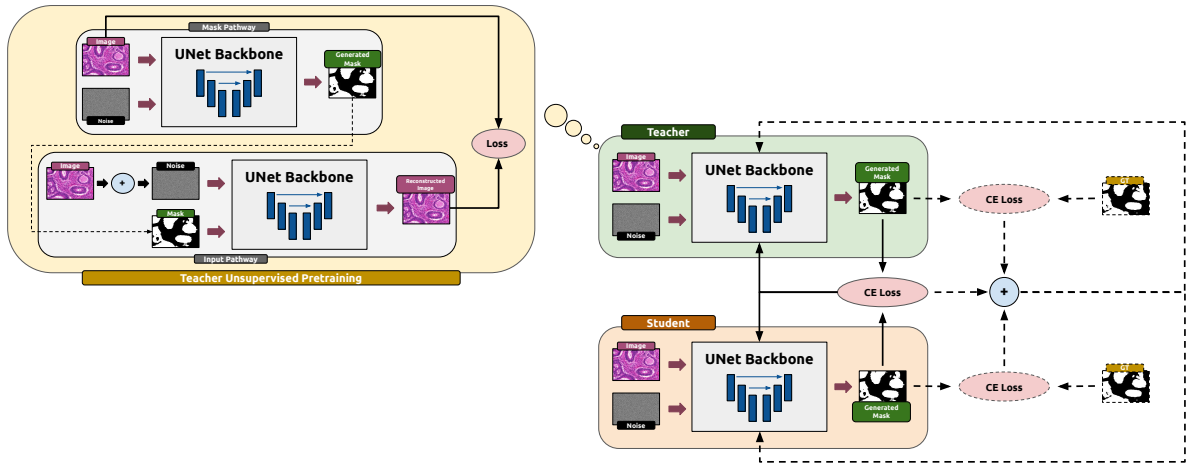


Figure 1: **Overview of the proposed teacher-student architecture for semi-supervised biomedical segmentation.** On the right, we depict the student-teacher co-training process, where both models are jointly optimized. Specifically, they are both based on a UNet architecture and draw inspiration from denoising diffusion probabilistic models (DDPMs), learning to generate semantic segmentation masks by starting from a noise vector conditioned on an input image. When ground-truth labels are available, both models are trained using a standard cross-entropy loss between predictions and the ground truth. In the absence of annotations, co-training is guided by cross pseudo-supervision (CPS), where the predictions of the teacher serve as pseudo-labels. To ensure that the teacher produces informative pseudo-labels, it undergoes a preliminary unsupervised training phase (shown on the left). This training follows a dual-pathway approach: first, it generates a segmentation mask from a noise vector conditioned on an input image, then reconstructs the original image using the generated mask and a noise-corrupted version of the input.

curate; however, under appropriate conditions, they can still enhance the performance of the student [26, 27]. Consequently, ensuring that the teacher produces high-quality outputs is essential for achieving optimal results. In semantic segmentation tasks, generating high-quality segmentation masks is particularly challenging, as these masks must not only assign class labels but also preserve the geometric and visual consistency of the image data [28, 29, 30].

In this paper, we introduce a novel semi-supervised teacher-student framework for biomedical semantic segmentation. Our approach leverages denoising diffusion probabilistic models (DDPMs), which have recently demonstrated remarkable success in modeling complex data distributions by progressively removing noise from corrupted samples [31, 32, 33]. As illustrated in Fig. 1, both the teacher and student networks adopt a UNet-based architecture and they harness these generative models to produce high-quality segmentation masks conditioned on input biomedical images. To enable the teacher model to generate informative pseudo-labels, we first employ an unsupervised pretraining strategy based on a cycle-consistency constraint, which enforces noise-corrupted image reconstruction. Specifically, it refines a noise sample conditioned on an input image to generate the corresponding segmentation mask. The generated mask is then combined with

a noise-perturbed version of the original image, and the model reconstructs the clean image, reinforcing its learning process. Once trained, the teacher is integrated into a semi-supervised learning framework alongside a student network. The two models are jointly optimized through a co-training process: the student generates segmentation masks conditioned on input images and is optimized using ground-truth labels when available and teacher-generated pseudo-labels otherwise, while the teacher iteratively improves its pseudo-labeling capabilities. Finally, to further enhance the stability and performance of the framework, we introduce a multi-round pseudo-label generation strategy. This iterative approach refines the co-training process, enabling the generation of more robust and reliable segmentation predictions.

We evaluate our methodology on three widely used public datasets for medical 2D image segmentation [10, 13, 14, 15], covering different imaging modalities and segmentation tasks. Specifically, we assess our approach on GlaS [34] for colorectal cancer segmentation in Hematoxylin and Eosin (H&E) stained histological images, PH2 [35] for skin lesion segmentation in dermoscopic images, and HMEPS [36] for pupil segmentation in grayscale eye images. Additionally, we extend our evaluation to volumetric data using the LA [37] dataset for left atrial segmentation in MRIs. We bench-

mark our method against several SOTA semi-supervised approaches based on pseudo-labeling and consistency training [23, 24, 38, 25, 29, 39]. Our results show that the proposed approach consistently achieves competitive performance across various levels of label scarcity, often reaching SOTA results.

Concretely, our contributions are as follows:

- We propose a novel semi-supervised learning framework for biomedical image segmentation based on DDPMs. Our approach follows a teacher-student paradigm and harnesses the capabilities of generative models for producing informative segmentation masks conditioned on input samples. First, the teacher learns to generate pseudo-labels by leveraging an unsupervised cycle-consistency constraint that enforces noise-corrupted image reconstruction. The student is then trained through a semi-supervised co-training process that integrates both ground-truth labels, when available, and teacher-generated pseudo-labels otherwise, while the teacher continuously refines its pseudo-labeling capabilities over time.
- We introduce a multi-round pseudo-label generation strategy, performed by the teacher, that enhances the semi-supervised teacher-student co-training by iteratively generating and refining pseudo-labels.
- We validate our methodology on multiple public biomedical imaging benchmarks, demonstrating that our approach significantly outperforms SOTA methods across various levels of label availability.

The rest of the paper is organized as follows: Sec. 2 provides an overview of related work in semi-supervised biomedical image segmentation. Sec. 3 details our proposed methodology. Sec. 4 presents our experimental evaluation and results. Finally, Sec. 5 concludes the paper.

2. Related Work

The rise of deep learning has driven the widespread use of CNNs and Transformers in semantic segmentation, leading to the development of models such as FCN [3], SegNet [40], and DeepLabV3 [2]. In the domain of biomedical imaging, UNet-like architectures have proven to be the most effective and widely adopted [12, 4, 6, 7, 11]. A major challenge faced by these approaches is the scarcity of labeled data. To overcome this limitation, semi-supervised learning provides

a compelling solution by leveraging large amounts of unlabeled data alongside a small set of labeled examples [41, 42]. Semi-supervised techniques generally fall into two main categories: pseudo-labeling methods and consistency-based methods.

Pseudo-labeling approaches. Pseudo-labeling methods have been a cornerstone of semi-supervised learning since early research in the field [27]. The core idea is to leverage a teacher model to generate surrogate labels (i.e., pseudo-labels) for data samples that lack ground-truth annotations. The student model is then trained in a supervised manner using these generated pseudo-labels. When pseudo-labels are of high quality, this approach can significantly enhance the performance of the student model, as demonstrated by several studies [16, 17]. In biomedical image segmentation, pseudo-labeling techniques have proven particularly effective. A simple yet intuitive approach is entropy minimization (EM) [27, 23], where the model generates its own pseudo-labels, which is mathematically equivalent to adding a loss term that encourages high-entropy output distributions [27]. A more advanced technique is the mean teacher (MT) framework [16], in which the teacher model shares the same architecture as the student but maintains weights as an exponential moving average of the student parameters across training iterations. The uncertainty-aware mean teacher (UAMT) method [24] further adapts this strategy for biomedical image segmentation by incorporating uncertainty estimation. Another notable approach is cross pseudo-supervision (CPS) [25], which employs two independently initialized networks that generate pseudo-labels for one another, enhancing robustness and generalization.

Consistency-based methods. Like pseudo-labeling methods, consistency-based techniques leverage the model’s own predictions as surrogate labels when ground-truth annotations are unavailable. However, instead of directly using the unaltered outputs of the model, these methods introduce perturbations – such as data augmentations, noise, or architectural variations – that modify the input or model itself. A consistency loss is then enforced to ensure that the model produces stable and coherent predictions across these perturbations, improving robustness and generalization [17, 43]. In biomedical image segmentation, several approaches have been developed following this principle. Cross-consistency training (CCT) [38] applies perturbations in the latent space representation of the input data and decodes multiple segmentation

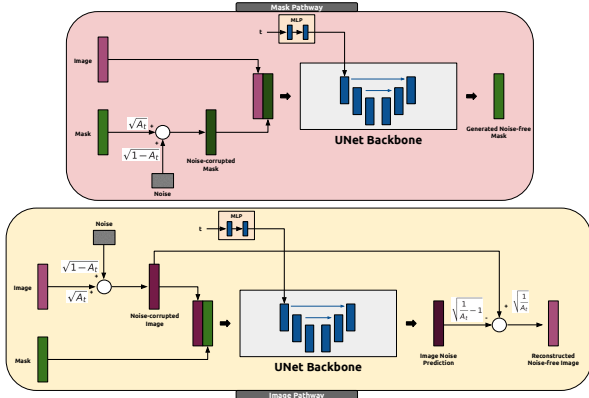


Figure 2: **Overview of the unsupervised teacher pretraining.** As with standard denoising diffusion methods, the architecture is based on a UNet model. However, we introduce two alternating computational pathways: (i) a mask pathway (top) and (ii) an image pathway (bottom). In the mask pathway, the network processes a noise-corrupted segmentation mask, concatenated with a clean input image, and aims to generate a noise-free mask. In the image pathway, the network receives a noise-corrupted image, concatenated with a clean mask, and is tasked with predicting the initial noise added to the image. Finally, the original image is then reconstructed following the approach in [31]. This reconstructed image is used to compute a cycle-consistency loss, allowing the teacher to generate meaningful masks conditioned on image samples.

maps from these perturbed versions. The model is trained under a consistency constraint, ensuring that the different segmentation outputs remain aligned. A different approach is taken by uncertainty rectified pyramid consistency (URPC) [29], which enforces consistency across multiple segmentation outputs generated at different stages of the network. This is achieved by placing linear decoders on top of each upsampling layer, producing distinct segmentation maps at various resolutions and ensuring agreement among them.

Contributions. Within the taxonomy outlined above, our proposed approach falls under the category of teacher-student pseudo-labeling methods. These methods are highly efficient and deliver strong learning performance. However, their effectiveness heavily depends on the quality of the generated pseudo-labels, particularly during the initial training phases, where low-quality labels can introduce biases into the learning process [44]. To address this challenge, we exploit state-of-the-art diffusion models [32, 33] as a means to enhance pseudo-label quality. Specifically, leveraging the principles of denoising diffusion probabilistic models (DDPMs) [31], we design a teacher model capable of generating informative pseudo-labels solely from unlabeled data. This teacher is then paired with an iden-

tical student model, enabling semi-supervised learning within a pseudo-labeling framework. Given that denoising diffusion models inherently rely on UNet-like architectures, they are particularly well-suited for biomedical image segmentation, where such backbones are widely adopted.

3. Method

Our approach to semantic segmentation of biomedical images follows a student-teacher framework and is built upon conditional denoising diffusion probabilistic models (DDPMs) [31]. Broadly, the teacher model generates pseudo-labels, which the student leverages during training in the absence of ground-truth annotations, enabling a semi-supervised learning strategy. To ensure reliable pseudo-label generation, we first conduct preliminary unsupervised training of the teacher, which is guided by a cycle-consistency constraint involving semantic mask generation and image reconstruction. In the following, we begin by detailing this unsupervised training phase before introducing our semi-supervised learning scheme, which is characterized by a co-training process between the teacher and the student. In this setup, the student learns to generate segmentation masks using ground-truth labels when available and teacher-provided pseudo-labels otherwise. Simultaneously, the teacher iteratively improves its pseudo-labeling capability. Finally, we outline our multi-round pseudo-label generation strategy, which further enhances the stability and performance of our method.

3.1. Unsupervised Teacher Pretraining

During the preliminary unsupervised training, the teacher features two distinct computational pathways operating alternatively: (i) an *image pathway* that processes the input image and (ii) a *mask pathway* that processes a segmentation mask (see also Fig. 2). Both pathways introduce noise into their inputs according to the principles of diffusion models. Formally, given an image i and its corresponding segmentation mask m , noise is added as follows:

$$\begin{aligned}\tilde{i} &= \sqrt{A_t} i + \sqrt{1 - A_t} v_i \\ \tilde{m} &= \sqrt{A_t} m + \sqrt{1 - A_t} v_m\end{aligned}\quad (1)$$

where v_i and v_m are Gaussian noise samples, i.e., $v_i \sim \mathcal{N}(0, I)$, $v_m \sim \mathcal{N}(0, I)$, and A_t controls the noise level and is determined by the diffusion time step parameter t , where a higher t corresponds to more noise addition

steps, resulting in noisier image and mask samples. For further details, we refer to [31].

In the mask pathway, the network processes a noise-corrupted segmentation mask concatenated with a clean input image and aims to reconstruct the original mask. Conversely, in the image pathway, the network receives a noise-corrupted image concatenated with a clean mask, with the ultimate goal of reconstructing the original image. However, rather than directly reconstructing the image, the network is trained to perform a proxy task: predicting the initial noise added to the image, from which the reconstruction is subsequently derived. Additionally, in both pathways, the UNet-based architecture incorporates the diffusion time step t as an additional input. This time step is processed through a multi-layer perceptron (MLP) to produce a latent representation, which is then added to the mask and image features. Formally, the outputs of the two pathways can be expressed as follows:

$$\begin{aligned}\hat{m} &= f_m(i, \tilde{m}, t) \\ \hat{v}_i &= f_i(\tilde{i}, m, t)\end{aligned}\quad (2)$$

where f_m and f_i denote the mask and image pathways, respectively, while \hat{m} represents the reconstructed segmentation mask and \hat{v}_i the predicted noise. The reconstructed image can then be obtained from the predicted noise following the approach in [31]:

$$\hat{i} = \sqrt{\frac{1}{A_t}} \tilde{i} + \sqrt{\frac{1}{A_t} - 1} \hat{v}_i \quad (3)$$

where \hat{i} denotes the reconstructed version of the original image. For clarity, in the following, we introduce the shorthand notation:

$$\hat{i} = f_i(\tilde{i}, m, t) \quad (4)$$

to compactly represent the computation performed by f_i , implicitly assuming the subsequent reconstruction of \hat{i} from the predicted noise.

These two pathways are utilized to establish a cycle-consistency loss for training the teacher model (see also Fig. 1). Specifically, in the mask pathway, instead of using a noise-corrupted segmentation mask as input, we replace it with a pure noise tensor v_m , which is obtained by adding noise to a zero tensor:

$$\hat{m} = f_m(s, v_m, t) \quad (5)$$

where, for each input, t is randomly sampled from a discrete uniform distribution $\mathcal{U}(0, T)$ (for a pre-defined maximum time step value T). The resulting output mask \hat{m} is then fed back to the teacher via the image pathway f_i , in its clean form, alongside a pure noise tensor serving as the input image:

$$\hat{i}' = f_i(v_i, \hat{m}, t') \quad (6)$$

Ultimately, to train the teacher model, we employ the following cycle-consistency loss:

$$\mathcal{L}^{(teacher)} = (i - \hat{i}')^2 \quad (7)$$

This loss ensures that the model reconstructs the original image, allowing it to leverage the underlying distribution of the unlabeled training data. Moreover, since the reconstruction process depends on the mask generated in the first forward pass, the output mask is encouraged to be *informative* about the original input. This training strategy enables the teacher to generate meaningful masks *conditioned* on image samples through f_i , and vice-versa, to generate image samples *conditioned* on masks via f_s . Once trained, the teacher is then capable of producing useful pseudo-labels for semi-supervised training of the student model. Some visualizations of teacher-generated pseudo-labels are included in Fig. 3.

3.2. Semi-supervised teacher-student co-training

The semi-supervised co-training process involves the mask pathway of both the teacher and student models, where each model generates a segmentation mask \hat{m} based on an input image i and a noise sample v_m (see also Fig. 1). Formally:

$$\begin{aligned}\hat{m}^{(teacher)} &= f_m^{(teacher)}(s, v_m, t) \\ \hat{m}^{(student)} &= f_m^{(student)}(s, v_m, t)\end{aligned}\quad (8)$$

where the notation follows the previous section.

To enforce consistency between the teacher and student predictions, we adopt a cross pseudo-supervision (CPS) [25] semi-supervised loss:

$$\begin{aligned}\mathcal{L}^{(semi)} &= \text{CE}(\hat{m}^{(student)}, \text{argmax}(\hat{m}^{(teacher)})) \\ &+ \text{CE}(\hat{m}^{(teacher)}, \text{argmax}(\hat{m}^{(student)}))\end{aligned}\quad (9)$$

where CE represents the standard pixel-wise cross-entropy loss, and argmax is applied along the channel dimension. This bidirectional supervision mechanism allows the segmentation prediction of the teacher

to guide the student while simultaneously enabling the prediction of the student to influence the teacher, allowing both models to refine their outputs iteratively.

Furthermore, when a ground-truth label l is available, we incorporate an additional supervised loss term:

$$\mathcal{L}^{(sup)} = \text{CE}(\hat{m}^{(teacher)}, l) + \text{CE}(\hat{m}^{(student)}, l) \quad (10)$$

In such cases, both teacher and student networks are directly optimized using the available annotations.

3.3. Multiple Rounds of Diffusion

In the previous section, while computing the co-training loss, we only leveraged the mask pathway of the teacher $f_m^{(teacher)}$ – along with the mask pathway of the student. To also incorporate the input pathway of the teacher $f_i^{(teacher)}$, we propose the following strategy. Specifically, after obtaining the mask $\hat{m}^{(teacher)}$, we use it as input to the teacher’s input pathway along with the noise-corrupted image \tilde{i} . This allows the model to generate a reconstructed version \hat{i}_1 of the original image, conditioned on the previously generated mask $\hat{m}^{(teacher)}$:

$$\hat{i}_1 = f_i^{(teacher)}(i, \hat{m}^{(teacher)}, t') \quad (11)$$

The reconstructed sample \hat{i}_1 is then used to generate a new mask \hat{m}_1 through $f_m^{(teacher)}$, conditioned on \hat{i}_1 :

$$\hat{m}_1 = f_m^{(teacher)}(\hat{i}_1, v_m, t'') \quad (12)$$

Due to the stochastic nature of the generative process, the newly generated mask \hat{m}_1 will differ slightly from the original $\hat{m}^{(teacher)}$. However, this discrepancy can be leveraged to encourage the teacher model to produce more informative pseudo-labels. To achieve this, we introduce an additional alignment loss term, ensuring that the output of the teacher \hat{m}_1 aligns with the same target as in Eq. 9 and Eq. 10:

$$\mathcal{L}_1^{(align)} = \text{CE}(\hat{m}_1, \hat{l}) \quad (13)$$

where \hat{l} corresponds to the ground-truth label l of the sample i , if available, or otherwise is defined as $\hat{l} = \text{argmax}(\hat{m}^{(student)})$. Additionally, we also introduce a reconstruction loss, similar to the cycle-consistency loss in Eq. 7, that exploits the reconstructed image \hat{i}_1 :

$$\mathcal{L}_1^{(reconstr)} = (i - \hat{i}_1)^2 \quad (14)$$

This process is repeated over multiple iterations, producing a diverse set of reconstructions $\hat{i}_1, \hat{i}_2, \dots, \hat{i}_R$ and corresponding masks $\hat{m}_1, \hat{m}_2, \dots, \hat{m}_R$ for a given

input image. We refer to this iterative approach as *multiple rounds of diffusion* and define R as the number of iterations of the generative process, and, for each round, we compute the corresponding losses $\mathcal{L}_1^{(reconstr)}, \mathcal{L}_2^{(reconstr)}, \dots, \mathcal{L}_R^{(reconstr)}$, and $\mathcal{L}_1^{(align)}, \mathcal{L}_2^{(align)}, \dots, \mathcal{L}_R^{(align)}$.

In the end, the overall loss exploited for the semi-supervised co-training of our teacher-student architecture is defined as:

$$\begin{aligned} \mathcal{L}^{(semi)} &= \lambda_{semi} \mathcal{L}^{(semi)} \\ &+ \lambda_{align} \frac{1}{R} \sum_{i=1}^R \mathcal{L}_i^{(align)} + \lambda_{reconstr} \frac{1}{R} \sum_{i=1}^R \mathcal{L}_i^{(reconstr)} \end{aligned} \quad (15)$$

when ground-truth annotations are not available, or

$$\begin{aligned} \mathcal{L}^{(sup)} &= \mathcal{L}^{(sup)} + \lambda_{semi} \mathcal{L}^{(semi)} \\ &+ \lambda_{align} \frac{1}{R} \sum_{i=1}^R \mathcal{L}_i^{(align)} + \lambda_{reconstr} \frac{1}{R} \sum_{i=1}^R \mathcal{L}_i^{(reconstr)} \end{aligned} \quad (16)$$

otherwise. The coefficients λ_{semi} , λ_{align} , $\lambda_{reconstr}$ are hyperparameters that determine the weight of each loss contribution. In practice, we set all these parameters to a fixed value λ . Following established practices in the semi-supervised literature [38, 24, 23, 29], this value is increased according to a linear schedule over the training epochs, until a maximum value λ_{max} is achieved in correspondence with the last epoch: $\lambda = \lambda_{max} \frac{\text{current_epoch}}{\text{max_epochs}}$.

4. Experiments and Results

4.1. Datasets and Evaluation Metrics

We evaluate our proposed method on three publicly available datasets commonly used in 2D biomedical image segmentation research [10, 13, 14, 15], covering different imaging modalities and segmentation tasks.

GlaS [34]. The gland segmentation in colon histology images challenge (GlaS) dataset consists of 165 histological images of colorectal adenocarcinoma stained with Hematoxylin and Eosin (H&E), each with a resolution of 775×522 pixels. The dataset is divided into 80 training images (37 benign, 43 malignant) and 85 test images (37 benign, 48 malignant).

PH2 [35]. This dermoscopic image dataset contains 200 melanocytic lesion images, categorized into 80 common nevi, 80 atypical nevi, and 40 melanomas. The images are captured as 8-bit RGB color images at a resolution

Labeled %	Method	GlaS		PH2		HMEPS	
		DC (%) \uparrow	JI (%) \uparrow	DC (%) \uparrow	JI (%) \uparrow	DC (%) \uparrow	JI (%) \uparrow
100%	Fully Sup.	90.62 \pm 0.20	82.85 \pm 0.34	92.44 \pm 0.38	85.96 \pm 0.66	96.98 \pm 0.42	94.70 \pm 0.43
1%	EM	68.92 \pm 0.77	52.60 \pm 0.90	73.24 \pm 2.32	57.92 \pm 2.87	90.24 \pm 2.74	82.25 \pm 4.52
	CCT	68.97 \pm 0.73	52.65 \pm 0.86	73.42 \pm 1.58	58.06 \pm 1.98	91.09 \pm 2.50	84.03 \pm 4.24
	UAMT	69.12 \pm 0.86	52.83 \pm 1.02	74.72 \pm 1.45	59.70 \pm 1.84	90.18 \pm 0.77	82.12 \pm 1.27
	URPC	68.38 \pm 0.44	51.96 \pm 0.51	71.23 \pm 1.95	55.39 \pm 2.33	89.15 \pm 0.79	80.45 \pm 1.28
	CPS	69.32 \pm 0.59	53.05 \pm 0.69	76.07 \pm 2.12	61.50 \pm 2.71	90.39 \pm 0.55	82.49 \pm 0.91
	Ours	70.03 \pm 1.80	53.92 \pm 2.14	78.18 \pm 1.34	64.21 \pm 1.83	91.69 \pm 0.19	84.66 \pm 0.33
2%	EM	70.23 \pm 1.34	54.16 \pm 1.60	79.34 \pm 2.63	65.95 \pm 3.55	91.35 \pm 1.93	84.14 \pm 3.19
	CCT	70.05 \pm 0.94	53.92 \pm 1.11	80.13 \pm 1.41	66.90 \pm 1.96	91.48 \pm 2.45	84.34 \pm 4.19
	UAMT	69.71 \pm 1.27	53.55 \pm 1.52	79.76 \pm 1.26	66.38 \pm 1.74	92.42 \pm 0.09	86.06 \pm 0.16
	URPC	68.67 \pm 0.98	52.31 \pm 1.17	78.88 \pm 1.69	65.22 \pm 2.33	89.78 \pm 0.64	81.47 \pm 1.05
	CPS	70.60 \pm 1.13	54.59 \pm 1.35	79.64 \pm 2.72	66.39 \pm 3.71	91.07 \pm 0.28	83.60 \pm 0.48
	Ours	72.22 \pm 2.09	56.58 \pm 2.54	81.51 \pm 1.74	68.84 \pm 2.49	92.86 \pm 0.46	86.69 \pm 0.80
5%	EM	75.34 \pm 0.92	60.45 \pm 1.17	81.89 \pm 1.02	69.37 \pm 1.44	92.31 \pm 1.07	85.78 \pm 1.84
	CCT	76.33 \pm 1.10	61.76 \pm 1.43	82.78 \pm 1.15	70.66 \pm 1.63	93.25 \pm 0.92	87.38 \pm 1.57
	UAMT	75.14 \pm 0.65	60.19 \pm 0.83	83.75 \pm 1.11	72.08 \pm 1.64	93.03 \pm 1.18	87.02 \pm 2.00
	URPC	74.32 \pm 1.06	59.17 \pm 1.34	83.41 \pm 2.17	71.65 \pm 3.14	90.85 \pm 0.72	83.23 \pm 1.22
	CPS	76.17 \pm 0.98	61.54 \pm 1.28	82.86 \pm 1.18	70.78 \pm 1.73	92.89 \pm 0.41	86.72 \pm 0.72
	Ours	77.30 \pm 1.90	63.01 \pm 2.52	86.15 \pm 0.98	75.69 \pm 1.52	93.79 \pm 0.23	88.12 \pm 0.27
10%	EM	78.08 \pm 0.82	64.06 \pm 1.10	84.94 \pm 0.90	73.85 \pm 1.35	92.56 \pm 0.96	86.20 \pm 1.65
	CCT	80.36 \pm 1.05	67.19 \pm 1.44	87.93 \pm 1.96	78.46 \pm 3.14	93.45 \pm 0.05	87.70 \pm 0.09
	UAMT	79.31 \pm 0.77	65.72 \pm 1.04	87.37 \pm 0.58	77.59 \pm 0.92	93.14 \pm 0.47	87.16 \pm 0.82
	URPC	78.59 \pm 1.39	64.78 \pm 1.85	88.06 \pm 0.40	78.89 \pm 0.45	90.96 \pm 0.83	83.44 \pm 1.40
	CPS	80.35 \pm 1.11	67.16 \pm 1.56	84.33 \pm 0.82	72.93 \pm 1.21	92.83 \pm 0.46	86.63 \pm 0.81
	Ours	80.06 \pm 1.25	66.69 \pm 1.73	89.45 \pm 0.90	80.94 \pm 1.47	94.12 \pm 0.19	88.90 \pm 0.34
20%	EM	81.20 \pm 0.80	68.38 \pm 1.13	86.30 \pm 0.87	75.92 \pm 1.33	93.04 \pm 0.59	87.00 \pm 1.02
	CCT	84.22 \pm 0.84	72.76 \pm 1.25	89.95 \pm 0.57	81.74 \pm 0.94	93.30 \pm 0.20	87.45 \pm 0.36
	UAMT	83.03 \pm 0.69	71.00 \pm 1.00	88.95 \pm 0.64	80.12 \pm 1.04	93.42 \pm 0.82	87.68 \pm 1.55
	URPC	82.34 \pm 2.07	70.12 \pm 2.84	91.73 \pm 0.80	84.71 \pm 1.36	91.30 \pm 1.44	84.05 \pm 2.47
	CPS	83.90 \pm 0.51	72.27 \pm 0.77	86.49 \pm 0.97	76.23 \pm 1.52	93.04 \pm 0.12	86.99 \pm 0.22
	Ours	84.55 \pm 0.85	73.23 \pm 1.27	92.42 \pm 0.42	85.90 \pm 0.73	94.37 \pm 0.28	89.32 \pm 0.51

Table 1: Comparisons with SOTA. The best results are in bold.

of 768 \times 560 pixels using the Tuebinger mole analyzer system with 20 \times magnification.

HMEPS [36]. The human and mouse eyes for pupil semantic segmentation (HMEPS) dataset comprises 11,897 grayscale images of human (4,285) and mouse (7,612) eyes, captured under infrared (IR, 850 nm) illumination. The pupil areas were manually annotated by five human experts using polygonal masks.

For evaluation, we report two commonly used metrics in biomedical image segmentation assessing pixel-wise segmentation accuracy, i.e., dice coefficient (DC) and jaccard index (JI) [29, 39, 4, 6]. Among these, DC is widely regarded as the gold standard metric for this task.

4.2. Comparison with SOTA

We conduct a quantitative evaluation of our approach against several SOTA semi-supervised methods, including both pseudo-labeling and consistency training strategies: EM [23], CCT [38], UAMT [24], CPS [25],

and URPC [29]. Additionally, we include a fully supervised baseline for reference. To ensure a fair comparison, we re-implemented these SOTA methods using a consistent experimental setup, employing the same UNet model as the underlying architecture. Our experiments explore multiple semi-supervised scenarios, training the models with 1%, 2%, 5%, 10%, and 20% of labeled images. The reported results represent the mean over ten independent runs, together with 90% confidence intervals. Additional experimental details can be found in Appendix A. Quantitative results are shown in Tab. 1 while qualitative outcomes are provided in Fig. 3.

Glas. The results indicate that the proposed approach achieves superior performance compared to other methods in most cases, considering both metrics. This advantage is particularly pronounced when label availability is very limited (1–5%), where our method consistently demonstrates stronger results. The only excep-

Labeled %	Method	DC (%) \uparrow	JI (%) \uparrow
100%	Fully Sup.	91.76 \pm 0.11	84.77 \pm 0.19
1%	EM	64.00 \pm 3.55	47.09 \pm 3.84
	CCT	61.12 \pm 6.87	44.27 \pm 7.19
	UAMT	60.42 \pm 4.56	43.39 \pm 4.56
	URPC	68.48 \pm 5.88	52.14 \pm 6.85
	CPS	71.69 \pm 9.41	56.57 \pm 10.80
	Ours	73.58 \pm 7.24	58.33 \pm 9.17
2%	EM	73.53 \pm 4.09	58.36 \pm 6.96
	CCT	75.49 \pm 2.67	60.63 \pm 3.45
	UAMT	74.80 \pm 5.18	59.93 \pm 6.42
	URPC	77.53 \pm 2.59	63.37 \pm 3.40
	CPS	83.65 \pm 2.40	71.91 \pm 3.58
	Ours	82.78 \pm 6.25	70.63 \pm 9.09
5%	EM	80.80 \pm 3.73	67.84 \pm 5.33
	CCT	84.70 \pm 0.27	73.47 \pm 0.42
	UAMT	84.22 \pm 3.67	72.80 \pm 5.41
	URPC	83.26 \pm 1.42	73.09 \pm 5.10
	CPS	87.31 \pm 3.66	77.48 \pm 5.78
	Ours	87.95 \pm 2.90	78.50 \pm 4.64
10%	EM	85.33 \pm 1.42	74.41 \pm 2.18
	CCT	88.11 \pm 1.18	78.75 \pm 1.89
	UAMT	88.95 \pm 0.22	80.09 \pm 0.37
	URPC	86.84 \pm 0.77	76.75 \pm 1.20
	CPS	89.57 \pm 0.84	81.12 \pm 1.37
	Ours	89.70 \pm 1.36	81.32 \pm 2.24
20%	EM	89.51 \pm 0.26	81.01 \pm 0.42
	CCT	90.74 \pm 0.58	83.05 \pm 0.97
	UAMT	90.91 \pm 0.64	83.34 \pm 1.07
	URPC	89.12 \pm 0.32	80.38 \pm 0.52
	CPS	90.41 \pm 0.88	82.51 \pm 1.47
	Ours	90.61 \pm 2.12	82.83 \pm 3.54

Table 2: Experiments with 3D images on the Left Atrial (LA) dataset. The best results are in bold.

tion occurs at 10% label availability, where, while our approach does not outperform all competing methods, it remains highly competitive.

PH2. In this case, the results demonstrate that our method achieves superior performance in terms of DC and JI metrics compared to all the considered state-of-the-art competitors across all levels of label scarcity. Notably, our approach attains performance comparable to the fully supervised baseline while utilizing only 20% of the available labels.

HMEPS. On this dataset as well, our method outperforms all state-of-the-art competitors across all levels of label scarcity in terms of DC and JI metrics. Also in this case, our approach achieves performance comparable to the fully supervised baseline while utilizing only 20% of the available annotations.

4.3. Ablation Studies

We conduct some ablation studies to evaluate the impact of different components of our method on performance. To this end, we consider the three benchmarks and all label scarcity settings, focusing on the DC metric.

Effect of the teacher pretraining. In this section, we analyze the impact of teacher pretraining by comparing results with and without it. As shown in Fig. 4, our findings demonstrate that a preliminary teacher setup consistently enhances performance across nearly all evaluated settings, with particularly notable improvements on the PH2 and HMEPS datasets.

Number of diffusion rounds R . Here, we analyze the effect of the parameter R , which controls the number of diffusion rounds in our strategy defined in Sec. 3.3. As shown in Fig. 5, while varying R has a marginal effect on DC performance in most cases, it plays a crucial role in stabilizing training. This is reflected in the confidence intervals, which generally shrink as R increases. Overall, $R = 5$ emerges as a reasonable trade-off between performance and computational cost, as further increasing R yields diminishing returns while increasing computational overhead.

4.4. Experiments with Volumetric Images

To demonstrate the adaptability of our approach to 3D medical imaging, we also evaluate it on the Left Atrial (LA) dataset [37]. This dataset consists of 100 3D MRI scans from the 2018 atrial segmentation challenge, with 80 images allocated for training and 20 for testing, following standard practices in the literature. Quantitative and qualitative results are presented in Tab. 2 and Fig. 3, respectively, while additional experimental details can be found in Appendix A. The findings align with our previous observations, as our method outperforms all competing approaches in almost all cases – not ranking first in two settings but still achieving competitive results, further validating its effectiveness in handling complex 3D medical data.

5. Conclusions

In this work, we introduce a novel semi-supervised biomedical image segmentation framework that combines diffusion models with a teacher-student co-training strategy. By leveraging the generative capabilities of diffusion models, our approach enhances pseudo-label quality, leading to improved segmentation performance in low-data scenarios. We evaluate our method

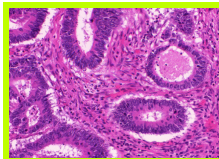




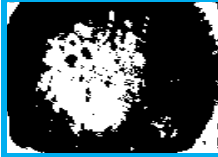






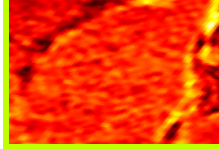



Dataset	Sample	Pseudo-label	Prediction	Target
GlaS				
PH2				
HMEPS				
LA (2D slice)				

Figure 3: Qualitative results from our semi-supervised approach in a 20% label scarcity setting. Each row corresponds to a different dataset we considered in our experimental evaluation; columns include a four-tuple sample–pseudo-label–prediction–target.

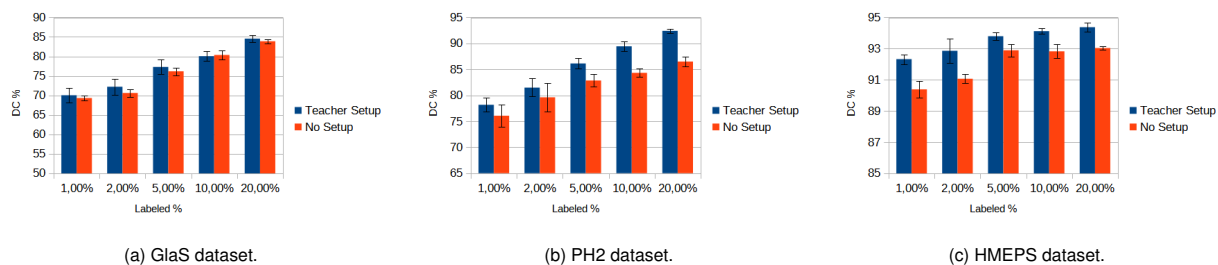


Figure 4: Ablation on the effect of teacher setup in SuperDiffusion. Results on various datasets under different degrees of label availability.

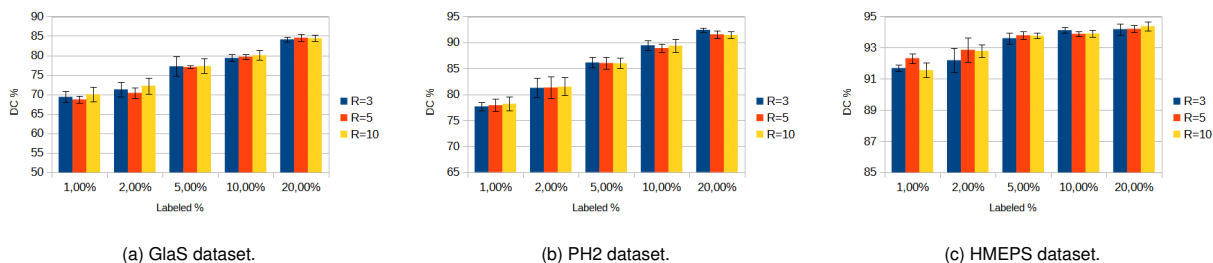


Figure 5: Ablation on the number of diffusion rounds R in our approach. Results are reported on various datasets under different levels of label availability.

on multiple public datasets for 2D medical image segmentation, including GlaS for colorectal cancer seg-

mentation in H&E-stained histological images, PH2 for skin lesion segmentation in dermoscopic images, and HMEPS for pupil segmentation in grayscale eye images. Additionally, we assess its applicability to 3D images using the LA dataset for left atrial segmentation in MRI scans, demonstrating its extensibility. Our results show that our method consistently outperforms several state-of-the-art approaches, achieving superior segmentation performance.

Overall, our findings underscore the effectiveness of integrating generative models with semi-supervised learning for biomedical image segmentation. By addressing the challenge of limited annotations, our approach enhances the reliability and data efficiency of segmentation models, highlighting its potential for broader applications in medical imaging. These results highlight the strong potential of diffusion models in semi-supervised biomedical image segmentation.

Acknowledgments

This work was partially funded by: Spoke 8, Tuscany Health Ecosystem (THE) Project (CUP B83C22003930001), funded by the National Recovery and Resilience Plan (NRRP), within the NextGeneration Europe (NGEU) Program; SUN – Social and hUman ceNtered XR (EC, Horizon Europe No. 101092612). We acknowledge the CINECA award under the ISCRA initiative, for the availability of high performance computing resources and support.

Appendix A. Experimental Details

All models used in our experiments were implemented in PyTorch. For the 2D datasets, we applied data augmentation techniques, including random vertical flips, random horizontal flips, and random rotations. Input images were resized to 128×128 for both training and inference. For the 3D setup, the same augmentation strategy was used during training. However, instead of resizing, we extracted random patches of size $96 \times 96 \times 80$ for training, which were then fed to the network. At inference time, patches of the same size were extracted using a sliding window approach with a 50% overlap.

Our approach was trained using the Adam optimizer for 200 epochs, with a learning rate of 0.01 and momentum coefficients of 0.9 and 0.99. A weight decay of $5 \cdot 10^{-5}$ was applied, with hyperparameters selected via grid search. Additionally, a learning rate schedule was

used, reducing the learning rate by a factor of 10 every 50 epochs. Hyperparameters for competing methods were chosen based on values reported in the literature. Additionally, For semi-supervised methods, the weight λ of the unsupervised loss contribution followed a linear schedule, as detailed in the main text, with a maximum value of $\lambda_{max} = 5$.

Finally, concerning the coefficient A_t used in the noise addition process, it was computed following standard denoising diffusion methods [31] as the cumulative product of coefficients $\beta_i = 1 - \alpha_i$ for $i = 1, \dots, t$:

$$A_t = \alpha_1 \alpha_2 \dots \alpha_t \quad (\text{A.1})$$

where each coefficient α_i represents the proportion of retained signal at time step i , while its complement (the diffusion rate) follows a standard linear schedule, ranging from $\beta_1 = 0.0001$ to $\beta_T = 0.02$. The total number of diffusion timesteps was set to $T = 1000$.

References

- [1] O. Ronneberger, P. Fischer, T. Brox, U-net: Convolutional networks for biomedical image segmentation, in: Medical Image Computing and Computer-Assisted Intervention – MICCAI 2015, Springer International Publishing, Cham, 2015, pp. 234–241. doi:10.1007/978-3-319-24574-4_28.
- [2] L. Chen, G. Papandreou, F. Schroff, H. Adam, Rethinking atrous convolution for semantic image segmentation, CoRR abs/1706.05587 (2017). arXiv:1706.05587.
- [3] J. Long, E. Shelhamer, T. Darrell, Fully convolutional networks for semantic segmentation, in: IEEE Conference on Computer Vision and Pattern Recognition, CVPR 2015, Boston, MA, USA, June 7-12, 2015, IEEE Computer Society, 2015, pp. 3431–3440. doi:10.1109/CVPR.2015.7298965.
- [4] F. Milletari, N. Navab, S. Ahmadi, V-net: Fully convolutional neural networks for volumetric medical image segmentation, in: 2016 Fourth International Conference on 3D Vision (3DV), IEEE Computer Society, Los Alamitos, CA, USA, 2016, pp. 565–571. doi:10.1109/3DV.2016.79.
- [5] Y. Xie, J. Zhang, C. Shen, Y. Xia, Cotr: Efficiently bridging cnn and transformer for 3d medical image segmentation, in: Medical Image

- Computing and Computer Assisted Intervention – MICCAI 2021, Springer International Publishing, Cham, 2021, pp. 171–180. doi:10.1007/978-3-030-87199-4_16.
- [6] A. Hatamizadeh, Y. Tang, V. Nath, D. Yang, A. Myronenko, B. Landman, H. R. Roth, D. Xu, Unetr: Transformers for 3d medical image segmentation, in: 2022 IEEE/CVF Winter Conference on Applications of Computer Vision (WACV), 2022, pp. 1748–1758. doi:10.1109/WACV51458.2022.00181.
- [7] H. Cao, Y. Wang, J. Chen, D. Jiang, X. Zhang, Q. Tian, M. Wang, Swin-unet: Unet-like pure transformer for medical image segmentation, in: Computer Vision – ECCV 2022 Workshops, Springer Nature Switzerland, Cham, 2023, pp. 205–218. doi:10.1007/978-3-031-25066-8_9.
- [8] L. Ciampi, G. Lagani, G. Amato, F. Falchi, A biologically-inspired approach to biomedical image segmentation, in: Computer Vision - ECCV 2024 Workshops - Milan, Italy, September 29-October 4, 2024, 2024, to appear.
- [9] L. Ciampi, G. Lagani, G. Amato, F. Falchi, Biologically-inspired semi-supervised semantic segmentation for biomedical imaging, CoRR abs/2412.03192 (2024). arXiv:2412.03192, doi:10.48550/ARXIV.2412.03192.
- [10] J. M. J. Valanarasu, V. A. Sindagi, I. Hacihaliloglu, V. M. Patel, Kiu-net: Overcomplete convolutional architectures for biomedical image and volumetric segmentation, IEEE Transactions on Medical Imaging 41 (4) (2022) 965–976. doi:10.1109/TMI.2021.3130469.
- [11] F. Isensee, P. F. Jaeger, S. A. A. Kohl, J. Petersen, K. H. Maier-Hein, nnu-net: a self-configuring method for deep learning-based biomedical image segmentation, Nature Methods 18 (2) (2020) 203–211. doi:10.1038/s41592-020-01008-z.
- [12] Ö. Çiçek, A. Abdulkadir, S. S. Lienkamp, T. Brox, O. Ronneberger, 3d u-net: Learning dense volumetric segmentation from sparse annotation, in: Medical Image Computing and Computer-Assisted Intervention – MICCAI 2016, Springer International Publishing, Cham, 2016, pp. 424–432. doi:10.1007/978-3-319-46723-8_49.
- [13] J. M. J. Valanarasu, P. Oza, I. Hacihaliloglu, V. M. Patel, Medical transformer: Gated axial-attention for medical image segmentation, in: Medical Image Computing and Computer Assisted Intervention – MICCAI 2021, Springer International Publishing, Cham, 2021, pp. 36–46. doi:10.1007/978-3-030-87193-2_4.
- [14] H. Basak, R. Kundu, R. Sarkar, Mfsnet: A multi focus segmentation network for skin lesion segmentation, Pattern Recogn. 128 (C) (aug 2022). doi:10.1016/j.patcog.2022.108673.
- [15] A. Karimi, K. Faez, S. Nazari, Deu-net: Dual-encoder u-net for automated skin lesion segmentation, IEEE Access 11 (2023) 134804–134821. doi:10.1109/ACCESS.2023.3337528.
- [16] A. Tarvainen, H. Valpola, Mean teachers are better role models: Weight-averaged consistency targets improve semi-supervised deep learning results, in: Advances in Neural Information Processing Systems 30: Annual Conference on Neural Information Processing Systems 2017, December 4-9, 2017, Long Beach, CA, USA, 2017, pp. 1195–1204.
- [17] A. Iscen, G. Tolias, Y. Avrithis, O. Chum, Label propagation for deep semi-supervised learning, in: IEEE Conference on Computer Vision and Pattern Recognition, CVPR 2019, Long Beach, CA, USA, June 16-20, 2019, Computer Vision Foundation / IEEE, 2019, pp. 5070–5079. doi:10.1109/CVPR.2019.00521.
- [18] V. Verma, K. Kawaguchi, A. Lamb, J. Kannala, A. Solin, Y. Bengio, D. Lopez-Paz, Interpolation consistency training for semi-supervised learning, Neural Networks 145 (2022) 90–106. doi:10.1016/J.NEUNET.2021.10.008.
- [19] T. Chen, S. Kornblith, K. Swersky, M. Norouzi, G. E. Hinton, Big self-supervised models are strong semi-supervised learners, Advances in neural information processing systems 33 (2020) 22243–22255.
- [20] C. Lee, J. Hong, C. Wu, J. Hou, Y. Lin, K. Huang, P. Tseng, Real-time coronary artery segmentation in CAG images: A semi-supervised deep learning strategy, Artif. Intell. Medicine 153 (2024) 102888. doi:10.1016/J.ARTMED.2024.102888.
- [21] C. Mei, X. Yang, M. Zhou, S. Zhang, H. Chen, X. Yang, L. Wang, Semi-supervised image segmentation using a residual-driven mean

- teacher and an exponential dice loss, *Artif. Intell. Medicine* 148 (2024) 102757. doi:10.1016/J.ARTMED.2023.102757.
- [22] J. Li, P. Zhang, X. Yang, L. Zhu, T. Wang, P. Zhang, R. Liu, B. Sheng, K. Wang, Ssmnet: Semi-supervised multi-task network for joint lesion segmentation and classification from pancreatic EUS images, *Artif. Intell. Medicine* 154 (2024) 102919. doi:10.1016/J.ARTMED.2024.102919.
- [23] T. Vu, H. Jain, M. Bucher, M. Cord, P. Pérez, ADVENT: adversarial entropy minimization for domain adaptation in semantic segmentation, in: *IEEE Conference on Computer Vision and Pattern Recognition, CVPR 2019, Long Beach, CA, USA, June 16-20, 2019, Computer Vision Foundation / IEEE, 2019*, pp. 2517–2526. doi:10.1109/CVPR.2019.00262.
- [24] L. Yu, S. Wang, X. Li, C.-W. Fu, P.-A. Heng, Uncertainty-aware self-ensembling model for semi-supervised 3d left atrium segmentation, in: *Medical Image Computing and Computer Assisted Intervention – MICCAI 2019, Springer International Publishing, Cham, 2019*, pp. 605–613.
- [25] X. Chen, Y. Yuan, G. Zeng, J. Wang, Semi-supervised semantic segmentation with cross pseudo supervision, in: *IEEE Conference on Computer Vision and Pattern Recognition, CVPR 2021, virtual, June 19-25, 2021, Computer Vision Foundation / IEEE, 2021*, pp. 2613–2622. doi:10.1109/CVPR46437.2021.00264.
- [26] C. Ouyang, C. Biffi, C. Chen, T. Kart, H. Qiu, D. Rueckert, Self-supervision with superpixels: Training few-shot medical image segmentation without annotation, in: *Computer Vision - ECCV 2020 - 16th European Conference, Glasgow, UK, August 23-28, 2020, Proceedings, Part XXIX, Vol. 12374 of Lecture Notes in Computer Science, Springer, 2020*, pp. 762–780. doi:10.1007/978-3-030-58526-6_45.
- [27] D.-H. Lee, et al., Pseudo-label: The simple and efficient semi-supervised learning method for deep neural networks, in: *Workshop on challenges in representation learning, ICML, Vol. 3, 2013*, p. 896.
- [28] Y. Zhou, J. Huang, C. Wang, L. Song, G. Yang, Xnet: Wavelet-based low and high frequency fusion networks for fully- and semi-supervised semantic segmentation of biomedical images, in: *IEEE/CVF International Conference on Computer Vision, ICCV 2023, Paris, France, October 1-6, 2023, IEEE, 2023*, pp. 21028–21039. doi:10.1109/ICCV51070.2023.01928.
- [29] X. Luo, G. Wang, W. Liao, J. Chen, T. Song, Y. Chen, S. Zhang, D. N. Metaxas, S. Zhang, Semi-supervised medical image segmentation via uncertainty rectified pyramid consistency, *Medical Image Analysis* 80 (2022) 102517. doi:https://doi.org/10.1016/j.media.2022.102517.
- [30] L. Luo, Architectures of neuronal circuits, *Science* 373 (6559) (2021) eabg7285. doi:10.1126/science.abg7285.
- [31] J. Ho, A. Jain, P. Abbeel, Denoising diffusion probabilistic models, in: *Advances in Neural Information Processing Systems 33: Annual Conference on Neural Information Processing Systems 2020, NeurIPS 2020, December 6-12, 2020, virtual, 2020*.
- [32] A. Kazerouni, E. K. Aghdam, M. Heidari, R. Azad, M. Fayyaz, I. Hacihaliloglu, D. Merhof, Diffusion models in medical imaging: A comprehensive survey, *Medical Image Anal.* 88 (2023) 102846. doi:10.1016/J.MEDIA.2023.102846.
- [33] H. Cao, C. Tan, Z. Gao, Y. Xu, G. Chen, P. Heng, S. Z. Li, A survey on generative diffusion models, *IEEE Trans. Knowl. Data Eng.* 36 (7) (2024) 2814–2830. doi:10.1109/TKDE.2024.3361474.
- [34] K. Sirinukunwattana, J. P. Pluim, H. Chen, X. Qi, P.-A. Heng, Y. B. Guo, L. Y. Wang, B. J. Matuszewski, E. Bruni, U. Sanchez, A. Böhm, O. Ronneberger, B. B. Cheikh, D. Racoceanu, P. Kainz, M. Pfeiffer, M. Urschler, D. R. Snead, N. M. Rajpoot, Gland segmentation in colon histology images: The glas challenge contest, *Medical Image Analysis* 35 (2017) 489–502. doi:https://doi.org/10.1016/j.media.2016.08.008.
- [35] T. Mendonça, P. M. Ferreira, J. S. Marques, A. R. S. Marcal, J. Rozeira, Ph2 - a dermoscopic image database for research and benchmarking, in: *2013 35th Annual International Conference of the IEEE Engineering in Medicine and Biology Society (EMBC), 2013*, pp. 5437–5440. doi:10.1109/EMBC.2013.6610779.

- [36] R. Mazziotti, F. Carrara, A. Viglione, L. Leonardo, L. V. Luca, B. Alessandro, R. Giulia, S. Giulia, A. Giuseppe, P. Tommaso, Human and Mouse Eyes for Pupil Semantic Segmentation (Feb. 2021). doi:10.5281/zenodo.4488164.
- [37] Z. Xiong, Q. Xia, Z. Hu, N. Huang, C. Bian, Y. Zheng, S. Vesal, N. Ravikumar, A. Maier, X. Yang, P.-A. Heng, D. Ni, C. Li, Q. Tong, W. Si, E. Puybareau, Y. Khoudli, T. Géraud, C. Chen, W. Bai, D. Rueckert, L. Xu, X. Zhuang, X. Luo, S. Jia, M. Sermesant, Y. Liu, K. Wang, D. Borra, A. Masci, C. Corsi, C. de Vente, M. Veta, R. Karim, C. J. Preetha, S. Engelhardt, M. Qiao, Y. Wang, Q. Tao, M. Nuñez-García, O. Camara, N. Savioli, P. Lamata, J. Zhao, A global benchmark of algorithms for segmenting the left atrium from late gadolinium-enhanced cardiac magnetic resonance imaging, *Medical Image Analysis* 67 (2021) 101832. doi:<https://doi.org/10.1016/j.media.2020.101832>.
- [38] Y. Ouali, C. Hudelot, M. Tami, Semi-supervised semantic segmentation with cross-consistency training, in: 2020 IEEE/CVF Conference on Computer Vision and Pattern Recognition, CVPR 2020, Seattle, WA, USA, June 13-19, 2020, Computer Vision Foundation / IEEE, 2020, pp. 12671–12681. doi:10.1109/CVPR42600.2020.01269.
- [39] X. Luo, J. Chen, T. Song, G. Wang, Semi-supervised medical image segmentation through dual-task consistency, *Proceedings of the AAAI Conference on Artificial Intelligence* 35 (10) (2021) 8801–8809. doi:10.1609/aaai.v35i10.17066.
- [40] V. Badrinarayanan, A. Kendall, R. Cipolla, Segnet: A deep convolutional encoder-decoder architecture for image segmentation, *IEEE Trans. Pattern Anal. Mach. Intell.* 39 (12) (2017) 2481–2495. doi:10.1109/TPAMI.2016.2644615.
- [41] Y. Bengio, P. Lamblin, D. Popovici, H. Larochelle, Greedy layer-wise training of deep networks, in: B. Schölkopf, J. Platt, T. Hoffman (Eds.), *Advances in Neural Information Processing Systems*, Vol. 19, MIT Press, 2006.
- [42] H. Larochelle, Y. Bengio, J. Louradour, P. Lamblin, Exploring strategies for training deep neural networks, *J. Mach. Learn. Res.* 10 (2009) 1–40.
- [43] K. Sohn, D. Berthelot, N. Carlini, Z. Zhang, H. Zhang, C. Raffel, E. D. Cubuk, A. Kurakin, C. Li, Fixmatch: Simplifying semi-supervised learning with consistency and confidence, in: *Advances in Neural Information Processing Systems 33: Annual Conference on Neural Information Processing Systems 2020, NeurIPS 2020*, December 6-12, 2020, virtual, 2020.
- [44] E. Arazo, D. Ortego, P. Albert, N. E. O’Connor, K. McGuinness, Pseudo-labeling and confirmation bias in deep semi-supervised learning, in: 2020 International Joint Conference on Neural Networks, IJCNN 2020, Glasgow, United Kingdom, July 19-24, 2020, IEEE, 2020, pp. 1–8. doi:10.1109/IJCNN48605.2020.9207304.